Modeling the circulation of Western Bank on the Scotian Shelf through sequential application of a variational algorithm and a nonlinear model

G. G. Panteleev,[1,2] B. de Young,[1] M. Luneva,[3] C. Reiss,[4] and E. V. Semenov[3]

Received 23 March 2003; revised 23 March 2003; accepted 5 August 2003; published 6 February 2004.

[1] A new approach is presented for the modeling of the quasi-stationary circulation through the sequential application of a variational algorithm and a nonlinear diagnostic model. The model loop begins with data assimilation of temperature, salinity, surface elevation, and velocity data in a simplified geostrophic model in which transport and continuity equations are treated as weak constraints. The temperature/salinity fields and balanced open boundary conditions points are then used as input to a nonlinear primitive equation model, which employs a turbulent closure scheme. The nonlinear model is then run to produce a diagnostic flow field. A radiation open boundary condition is applied at the outflow points of the open boundaries. These two steps are organized into an iteration cycle by using output from the nonlinear model as input to the variational model. The proposed approach combines the advantages of variational data assimilation in simplified models with a complicated fully nonlinear primitive equation model. We apply the approach to Western Bank on the Scotian Shelf. Comparisons with observed current from Western Bank, in September and October 1998, show that the sequential application of the variational approach and the fully nonlinear model allow determination of the quasi-stationary circulation whose agreement with the observations is $\approx$10–30% better than circulation determined from the variational or the nonlinear model alone. Our calculations of the cross-shelf transport across Western Bank show that it varies from 0.20 Sv to 0.35 Sv over a 2-week period. The combined models also allow us to determine the character of the circulation over the Bank, the role of wind forcing and the implications for resident biological populations. *INDEX TERMS:* 4219 Oceanography: General: Continental shelf processes; 4255 Oceanography: General: Numerical modeling; 4223 Oceanography: General: Descriptive and regional oceanography; 4263 Oceanography: General: Ocean prediction; *KEYWORDS:* numerical modeling, Scotian Shelf, variational algorithm, shelf circulation

Citation: Panteleev, G. G., B. de Young, M. Luneva, C. Reiss, and E. V. Semenov (2004), Modeling the circulation of Western Bank on the Scotian Shelf through sequential application of a variational algorithm and a nonlinear model, *J. Geophys. Res.*, *109*, C02003, doi:10.1029/2003JC001868.

1. Introduction

[2] Determination of the quasi-stationary, or mean, circulation is a common challenge in oceanography. Despite some formal mathematical differences, the problem is traditionally solved via diagnostic calculation of the circulation from a given temperature/salinity distribution. The diagnostic velocity field provides an approximation to the quasi-stationary solution. This approach is well-established with a venerable history in numerical oceanography going back to *Helland-Hansen* [1934] through to *Sarkisyan* [1954], *Holland and Hirshman* [1972], *Csanady* [1979], and *de Young et al.* [1993]. The original concept, while quite straightforward, has been updated to allow incorporation of information on forcing, friction, and boundary conditions [*de Young et al.*, 1993; *Sheng and Thompson*, 1996]. The option to incorporate sophisticated high-resolution numerical models is an attractive feature of this method. At the same time, the inability to take into account a wide variety of different data types and errors in the observations create potential problems in the analysis of the results. These problems arise from the requirement for initial interpolation of the irregularly distributed temperature and salinity fields onto a regular grid. Many different interpolation techniques have been applied [e.g., *Bretherton et al.*, 1976], but even those based upon optimal interpolation [*Gandin*, 1963] can be subjective because of the need to define spatial correlation functions. Although there are techniques for calculating the correlation function from the data, some subjectivity is involved, particularly in regions

[1]Department of Physics and Physical Oceanography, Memorial University of Newfoundland, St. John's, Newfoundland, Canada.
[2]Also at Shirshov Institute of Oceanology, Moscow, Russia.
[3]Shirshov Institute of Oceanology, Moscow, Russia.
[4]Department of Oceanography, Dalhousie University, Halifax, Nova Scotia, Canada.

0148-0227/04/2003JC001868

with substantial anisotropy. For example, when applied on the continental shelf, optimal interpolation should retain the narrow density fronts often observed at the edges of the banks, but at the same time interpolation will smooth high-frequency disturbances of the thermocline caused by internal tides or waves [*Simpson*, 1998]. If these phenomena have the same spatial scale, then the direct implementation of optimal interpolation can become quite difficult, because the interpolation is trying to reconcile two incompatible inputs.

[3] Proper specification of the open boundary conditions is a problem common to all limited area models. The incorporation of different schemes for the radiation open boundary conditions [*Orlanski*, 1976; *Camerlengo and O'Brien*, 1980; *Greatbatch and Otterson*, 1991] only partly resolves the problems with outflow boundaries. Application of the zero net transport correction, after incorporation of the radiation boundary conditions schemes, can be done in different ways and can change inflow sections to outflows or vice versa. Optimization of the open boundary conditions, proposed by *Shulman and Lewis* [1995], is an effective way to overcome the open boundary problem, but the simultaneous determination of the velocity, salinity, and temperature boundary conditions [*Shulman et al.*, 1999] is rather complicated because of the nonlinearity of the governing equations.

[4] Both the interpolation and open boundary problems can be treated by applying variational or optimal control techniques [*Marchuk and Penenko*, 1979; *Le Dimet and Talagrand*, 1986; *Thacker and Long*, 1988]. In addition to permitting incorporation of different types of data and their errors, these approaches allow determination of a mathematically consistent quasi-stationary circulation. Recently, these techniques have been successfully applied in different regions with models of varying complexity [*Wunsch*, 1994; *Nechaev and Yaremchuk*, 1995]. Unfortunately, application of the data assimilation scheme with full nonlinear constraints requires not only powerful computers but also substantial amounts of data. The computational limitation is becoming less important, but the oceanographic data limitations are more difficult to overcome. In addition, sparse and irregularly distributed data can cause the Hessian matrix to be ill conditioned [*Thacker*, 1989].

[5] It is also likely that the strong nonlinearity of some models, for example turbulent closure models [*Mellor and Yamada*, 1982; *Launder et al.*, 1975], can lead to data assimilation problems because of the resulting complicated character of the cost function; however, these models do also permit substantial improvements in the upper layer circulation [*Semenov and Luneva*, 1996, 1999].

[6] An incremental approach, using a ''simple'' model for the definition of the cost function gradient, has recently been suggested [*Courtier et al.*, 1994; *Thompson et al.*, 2000]. The idea is to limit the influence of nonlinearity on the assimilation problem. With this approach, both the simple and the ''complicated'' models used must have the same control vector. *Thompson et al.* [2000] showed that the incremental approach is not necessarily convergent in practice and that the formulation for the adjoint code may be quite complicated even for a simple model.

[7] In this paper, we attempt to combine advantages of the variational data assimilation technique with traditional diagnostic calculation based on a sophisticated fully nonlinear model. Our algorithm is based on the sequential application of a simplified variational and a fully nonlinear model. The basis for the proposed integration and a description of the models are outlined in the next section.

[8] One of the reasons for the development of this model was the need to define the circulation on Western Bank, as part of a multi-disciplinary study. In this paper, we present the results of the model applied to temperature/salinity data obtained on Western Bank located in the outer Nova Scotia shelf region (Figure 1). Studies of the biology and circulation of Western Bank region were carried out during the summer and fall of 1997 and 1998. Two large-scale surveys of Western Bank were conducted in September–October 1998 (Figure 1). These surveys included direct velocity measurements at 11 mooring sites around the crest (Figure 1, top) within a square 80 km by 80 km and maintained for a 2.5-month period from August until mid-October. The data from the moorings were used to define the circulation of this area of the Scotian Shelf and also for testing our numerical approach.

[9] A discussion of the primary features of the Western Bank circulation and available data follows section 2. We then test our proposed approach by applying the model to data from Western Bank and then use the model results to define and explore aspects of the circulation of Western Bank. We conclude with a brief discussion of the strengths and weaknesses of the approach and a brief summary of the insights gained into the Western Bank circulation.

2. Methods

2.1. Approach

[10] We assume that we need to calculate quasi-stationary circulation in some region of the ocean and have at our disposal two models: a sophisticated diagnostic fully nonlinear model that adequately describes oceanic processes and a simplified variational model that can assimilate different data types taking into account their inherent errors. The quasi-stationary circulation can be determined from a diagnostic calculation alone using a fully nonlinear model, but the calculation suffers from limited data, the quality of the data interpolation, and the uncertain specification of the open boundary conditions. The variational data assimilation technique is free from these drawbacks but suffers from overly simplified dynamics. Even with these simplified dynamics, however, the temperature/salinity distribution, output from the variational model, should be more realistic than results from optimal interpolation because of the physically reasonable constraints used for the interpolation rather than simply applying a correlation function based upon imperfect data.

[11] Let us suppose that we can obtain results close to the observed initial temperature/salinity distribution and open boundary conditions by using the variational algorithm. Then, because of the superiority of the fully nonlinear model over the simplified constraints of the variational model, we might expect that the diagnostic calculation, a fully nonlinear model, should produce better results than does the variational data assimilation algorithm. At the same time, if the results of the diagnostic calculation with the nonlinear model are better than the results from the variational model, then it seems logical to use these results as

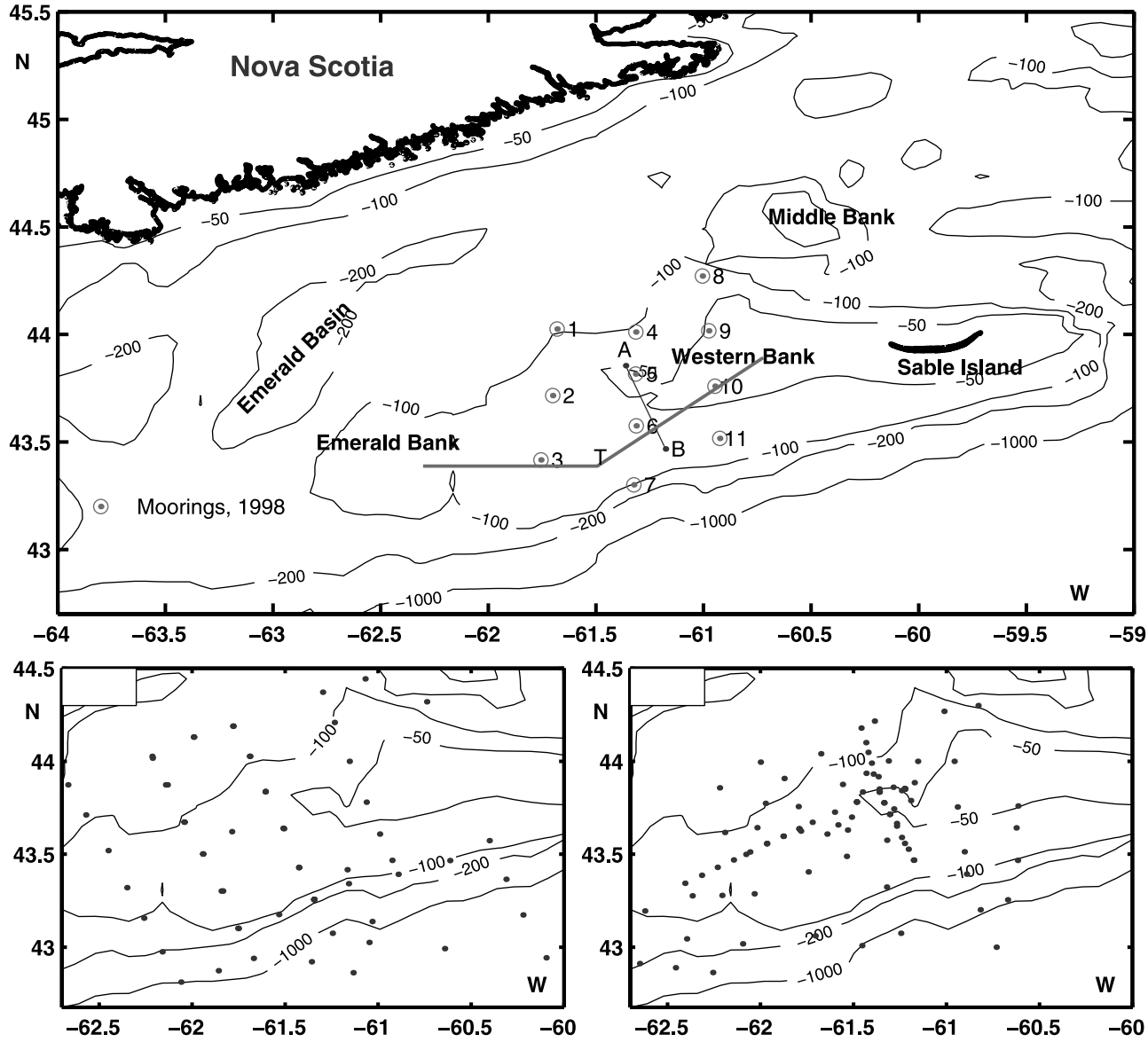

Figure 1. (top) Map of the Scotian shelf region showing the study area, locations of the moorings, and CTD stations occupied from 29 September to 20 October 1998. AB-line: position of the across bank transect; T-line: position of the T transect used for onshore transport estimates. (bottom) Locations of CTD profiles of first (bottom left) and second (bottom right) large-scale surveys.

additional "data" which, when combined with direct observations, can improve the output of the variational model.

[12] It is quite common that the observations are incomplete and so the number of degrees of freedom of the variational model is much larger than that for the available data. Another advantage of coupling the two models is that output from the nonlinear model introduces realistic information about the spatial distribution of the model variables into the variational model. Because oceanic observations are usually sparse and their statistics are unknown, or poorly known, such information can be crucial to improving the model output. As an example, *Legler et al.* [1989] used historical "climate" data to enhance convergence in their model solution of the Indian Ocean circulation.

[13] These ideas naturally lead to the organization of the outer iteration cycle (Figure 2). Following this schematic, as a first step, all available data with estimates of their error covariance should be assimilated into the variational data assimilation model. As a second step, output (the distribution of temperature/salinity and the open boundary conditions) of the variational model is incorporated into the diagnostic calculation using a fully nonlinear model. Results of the diagnostic calculation with prescribed error covariance are then fed back into the variational model to provide additional simulated data for that model. The cycle may be repeated several times.

[14] Obviously, the appropriate specification of the error covariance of the simulated data allows for some subjectivity in the approach, but for the newly simulated data D_{new} corresponding to analogous measurements D_{real}, it is natural to estimate the variance from

$$\sigma_{new} > \| D_{new} - D_{real} \| + \sigma_{real}. \quad (1)$$

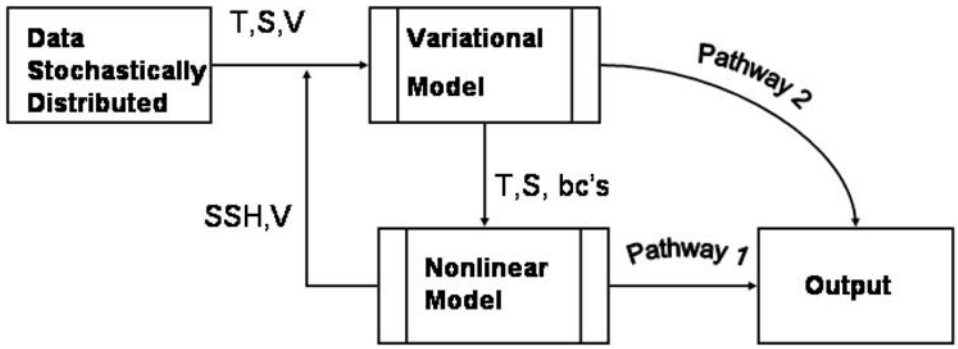

Figure 2. Schematic representation of the sequential application of the variational and nonlinear models.

This condition should ensure appropriate convergence to the observations at points where we have observations.

[15] Unfortunately, this scheme is based only on our physical Intuition, and convergence cannot be guaranteed. Moreover, because we are trying to treat non-stationary data with stationary models, and because of the differences between these models, the output of the nonlinear diagnostic model may partly contradict the variational model and/or the real non-stationary data. In such a situation, assimilation of that output might not be helpful and could produce worse results than from an earlier point in the outer iteration cycle. Possible reasons for divergence of the iteration cycle and ways to limit it are presented and discussed later in the paper. In the next two subsections, we describe the nonlinear and variational models that we have used.

2.2. Variational Data Assimilation Model

[16] As a simplified variational model we apply an algorithm previously utilized for the definition of the large-scale circulation in Southern Ocean [*Nechaev et al.*, 1997; *Grotov et al.*, 1998] The algorithm permits the assimilation of stochastically distributed temperature, salinity, sea surface height (SSH), horizontal velocity, wind stress, and atmospheric heat/salt fluxes data into a quasi-geostrophic stationary model where transport and continuity equations are treated as weak constraints [*Sasaki*, 1970]. This allows the dynamical equations to be applied with errors defined by the corresponding weight functions. Physically, these errors can be prescribed to represent some defined level of non-stationarity in the data and our limited knowledge of physical processes in lower boundary layers. Such modifications of the dynamical constraints permit us to avoid boundary control problem with the elliptic equation for the SSH which can be ill-conditioned [*Thacker*, 1987], but otherwise demand estimates of SSH spatial distribution.

[17] The major goal of including SSH estimates is to account for the barotropic component of the current in the variational model [*Nechaev et al.*, 1997]. Real velocity measurements could be used rather than SSH estimates, however, velocity measurements are less generally available and non-uniformly distributed.

[18] The errors arising from the dynamical equations of the variational model can be minimized by selecting the appropriate weight functions. From previous experiments, we have found that departures from the exact dynamical equations are critical primarily near abrupt changes in bottom topography.

[19] This model is valid for the large-scale, quasi-stationary circulation. Typically, for the outer Scotian Shelf, the spatial (50 km) and velocity (10 cm s^{-1}) scales yield a Rossby number of about Ro = 0.02, so the influence of the nonlinear terms in the momentum equation should be weak. *Han et al.* [1997] conclude that the baroclinic circulation is dominant over the Scotian Shelf; therefore, we expect that the variational model should be appropriate for calculation of the subtidal circulation on Western Bank. Our model is a modification of the large-scale version of [*Grotov et al.*, 1998] and includes different specifications of the vertical and horizontal diffusivity, but is formulated in terms of temperature and salinity rather than density. Using temperature and salinity is important because of the complicated water mass structure of the Scotian Shelf region [*Houghton et al.*, 1978].

[20] The proposed data assimilation algorithm yields dynamically balanced fields of assimilated data on a regular grid. This model allows us to interpolate stochastic data onto a regular grid and generate open boundary condition data consistent with the observations through the use of dynamical constraints.

[21] The variational data assimilation technique can be formulated as the minimization of the cost function defined on the manifold determined by the selected dynamical constraints. This yields a traditional least squares problem, and any constituents of such a cost function should be normalized by the corresponding error covariance function [*Wunsch*, 1996]. For δ-correlated Gauss-Markov processes, such error covariance functions are related to the variance of the corresponding constituents of the cost function. More detailed description of the governing equations and specification of the error covariance are given in Appendix A.

2.3. Nonlinear Model

[22] For the nonlinear model, we used a fully nonlinear primitive equation model [*Semenov and Luneva*, 1996, 1999]. that employs a $\kappa - \varepsilon$ turbulent closure scheme for the vertical eddy viscosity. The model includes the fully nonlinear 3-D shallow water equations for which we make the hydrostatic and Boussinesq assumptions. On the bottom and at the rigid walls, the velocity is set to zero and there is no diffusion of heat or salt. A kinematic boundary condition is applied to the vertical velocity at the surface. Horizontal

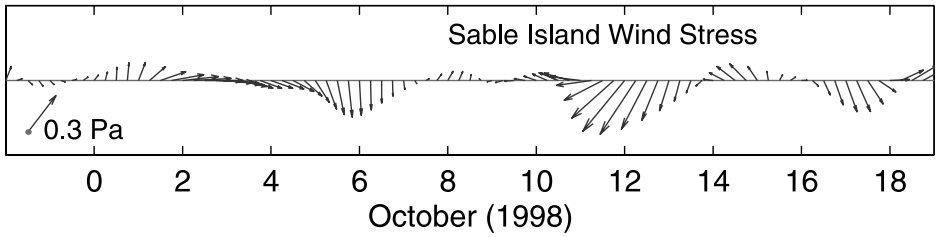

Figure 3. Wind stress time series for Sable Island.

velocities were specified at the inflow points of the open boundaries while an Orlanski radiation condition [*Orlanski*, 1976] was applied on the outflow points thus allowing for the free outflow of disturbances.

[23] The finite-difference approximation was based on the three-layer, leap-frog and (periodically turned on) Lax-Wendrof schemes [*Haidvogel and Beckmann*, 1999] in time with a C-grid in space. The Coriolis terms were approximated following *Delekluze and Zalesniy* [1996], who showed that for the C-grid the best approximation of the Coriolis and other terms of the momentum equation requires appropriate averaging in order to avoid grid-scale noise. We used the $\kappa - \varepsilon$ turbulence model of *Launder et al.* [1975]. The applicability of the model in this case is limited by the parameterization of subgrid processes in which the generation of turbulent energy is controlled by shear in the mean velocity, density gradients, and turbulence fluxes that are determined by the nonlinear model.

[24] The diagnostic calculation is developed as the stationary solution to the non-stationary nonlinear equations forced by stationary wind stress with fixed temperature and salinity fields. We define the stationary solution as having a constant level of energy. Because the temperature and salinity fields were fixed, the $\kappa - \varepsilon$ turbulent closure scheme influences only the velocity.

3. Application to Western Bank

[25] Our work on Western Bank required the development of some understanding of the quasi-stationary circulation for application to the dispersal and retention of biological organisms on and around the bank [*Reiss et al.*, 2000]. We deployed an array of current meters on the bank and ran several intensive cruises in the fall of 1998. We developed the modeling approach presented above to aid in our understanding of the circulation of the bank and to assist in the interpretation of the data. Here we use the data both to drive and to test the modeling approach and to determine the strengths and weaknesses of the models. We begin with a description of the data that we collected and some of the characteristics of the circulation on Western Bank and then finish this section with the modeling results and their analysis.

3.1. Observations on Western Bank

[26] From 29 September to 22 October 1998, we collected 158 CTD profiles around Western Bank (Figure 1). Fifty-seven of them were collected from 29 September to 6 October, a period we will call the first large-scale survey (first LSS) and 64 from 13 October to 20 October, the second large -scale survey (second LSS) (see Figure 1). Unfortunately, because of strong winds, neither survey completely covered the bank and surrounding regions.

[27] Most of the CTD profiles were obtained in depths less than 300 m. For the small number of CTD stations at depths greater than 300 m, we used historical data [*Petrie et al.*, 1996] to extend the profiles from 300 m to 1000 m depth. We extrapolated the profiles down to 1000 m, using polynomial interpolation applied to the historical data at 500, 700, and 1000 m. Note that any possible disagreement between the historical data and observations below 300 m depth is not critical for our domain since less than 10% of the region is deeper then 300 m, and the focus of our analysis is on the upper layer circulation (shallower than 100 m).

[28] Eleven moorings, with 25 current meters, were deployed over the western half of Western Bank (Figure 1), providing direct measurements from 2 August to 16 October. We used InterOcean S4 current meters for all the near-surface instruments (shallower than 40 m) with S4's and a few Aanderaa RCM7's for the deeper locations. Velocity data averaged over the period of the first LSS were used both for modeling and for model-data comparison. The current meters were recovered about a week before the end of the cruise because of weather conditions, so mean velocities observed during 13–16 October were used only for the model-data comparison.

[29] Wind stress from Sable Island, calculated following *Large and Pond* [1981], shows that there was a significant change in the mean wind stress between the first and second LSS (Figure 3). The mean wind during the first LSS was 0.14 Pa towards the east with a peak stress of 0.3 Pa. During the second LSS, the mean wind stress was 0.06 Pa towards the east with a peak stress of 0.24 Pa. Between the two surveys, the mean wind stress was 0.15 Pa towards the southwest with a peak stress of 0.5 Pa. Only the averaged wind stress for each of the two periods was used.

[30] As mentioned above, application of the variational model requires estimates of the SSH distribution, data unfortunately not available for Western Bank. In their absence, we used estimates of dynamic height relative to 500 m calculated following a modification of the Helland-Hansen dynamical method [*Sheng and Thompson*, 1996]. This method is valid where the bottom density does not vary along isobaths, a condition that holds for most of the Scotian Shelf. There is, however, some violation of this condition for Western Bank [see *Sheng and Thompson*, 1996, Figure 11]. Analysis of bottom density distribution during the first and second LSS revealed approximately 0.1–0.3 kg m^{-3} difference between bottom density on the northern and southern parts of the bank (Figure 4) below 80–100 m depth. Because the depth is less than 300 m over

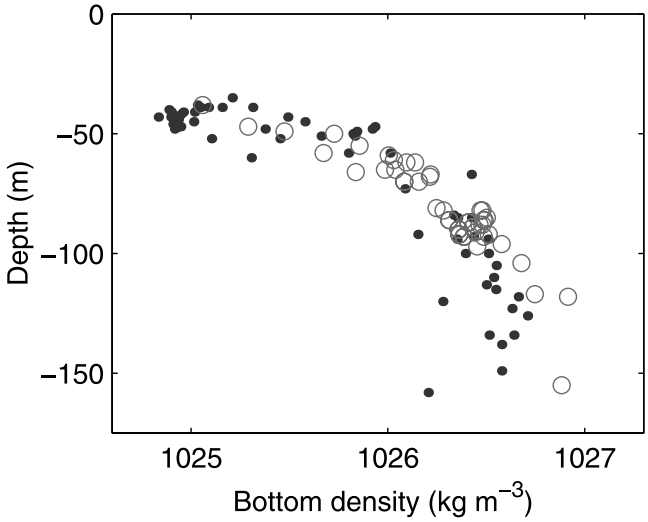

Figure 4. Bottom density against water depth for the northern (solid dots) and southern (circles) sides of the Western Bank.

most of our region, the estimated error of the dynamic SSH using this method is less than 0.03–0.05 m in water deeper than 100 m.

3.2. Western Bank Features

[31] Western Bank is an important bank in the system of banks that make up the Scotian Shelf [*Smith and Schwing*, 1991]. The bank is relatively large, located near the shelf break (Figure 1), and very productive biologically [*Reiss et al.*, 2000]. A broad channel along the southwestern edge of the bank, between Western Bank and nearby Emerald Bank, provides a conduit for the penetration of oceanic water onto the Scotian Shelf where it mixes with water coming along the shelf and water coming from the Emerald Basin. This is an important region for the determination of water properties on the Scotian Shelf since at least four water masses meet here [*Houghton et al.*, 1978].

[32] Recent work [*Thompson and Sheng*, 1997; *Han et al.*, 1997] has revealed that the circulation on the Scotian Shelf is regulated by three primary factors: wind-driven currents, tidal currents, and subtidal density-driven currents. Work by *Han et al.* [1997] showed the dominant influence of the density driven component (up to 97%) across a transect spanning the crest of Emerald Bank.

[33] The dominant tidal constituent, the semi-diurnal M_2 on the Bank has an amplitude of about 0.2 m s^{-1}; the diurnal K_1 constituent is much weaker with an amplitude of 0.05–0.1 m s^{-1}. Analysis of current data from the 11 moorings shows that the tides are primarily barotropic, except on the northern flank of Western Bank where there is evidence of an internal tidal response, revealed by a change in phase with depth. According to *Han et al.* [1997], M_2 tidal rectification in the central part of the Scotian Shelf is responsible for only 1–2% of the local along-shore transport.

[34] Although the tidal velocities are relatively large, water mass analysis, particle tracking from numerical modeling [*Griffin and Thompson*, 1996] and analysis of surface drifter data [*Sanderson*, 1995] show that for the periods in which we will be interested, 5- to 10-day subtidal periods, the advection of the density field, particularly during the summer, is not particularly important.

[35] The spatial decorrelation scale of the subtidal current velocity is about 30–35 km [*Thompson and Griffin*, 1998; *Panteleev et al.*, 2001], and the subtidal circulation in the regions close to the Western Bank is fairly stable. There is strong topographic steering and a persistent along slope westward current. Averaged velocities for the periods 25–30 September 1998 and 30 September to 5 October 1998 (Figures 5a and 5b) reveal that the primary features of the flow field are preserved between the two periods. Although the velocity amplitude changes by roughly 35%, the mean current direction only changes by about 20°.

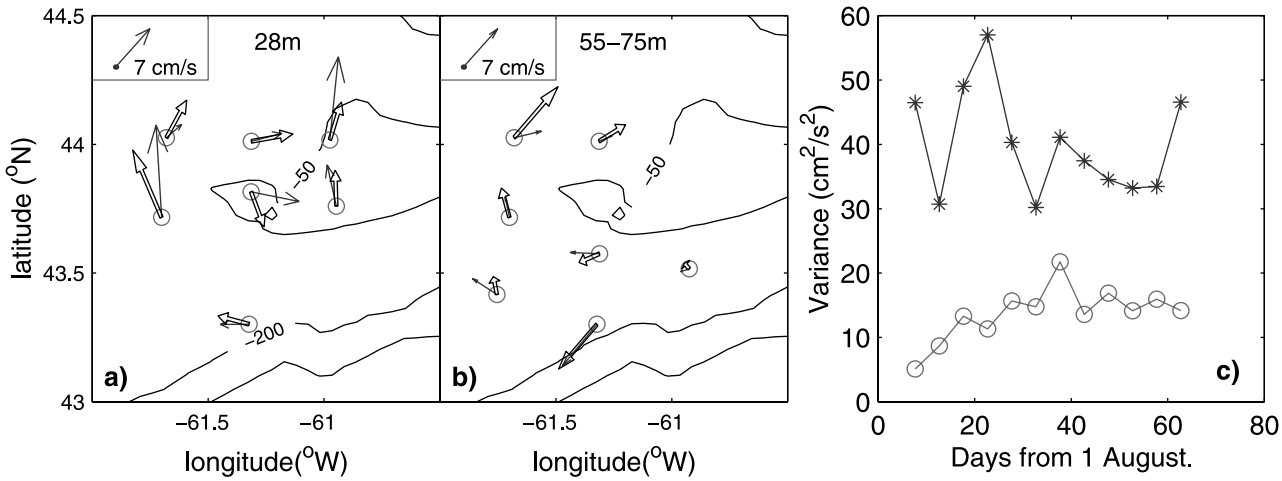

Figure 5. Averaged velocities over the two different periods 25–30 September (thin arrows) and 30 September to 5 October (thick arrows) at (a) 28 m and (b) 55–75 m depth. The current meter at the fifth mooring was deployed at 20 m depth and therefore was strongly influenced by wind stress. (c) Spatial running 5-day mean variance (asterisk) and average 5-day running subtidal variance (circles) on the Western bank for August–October 1998.

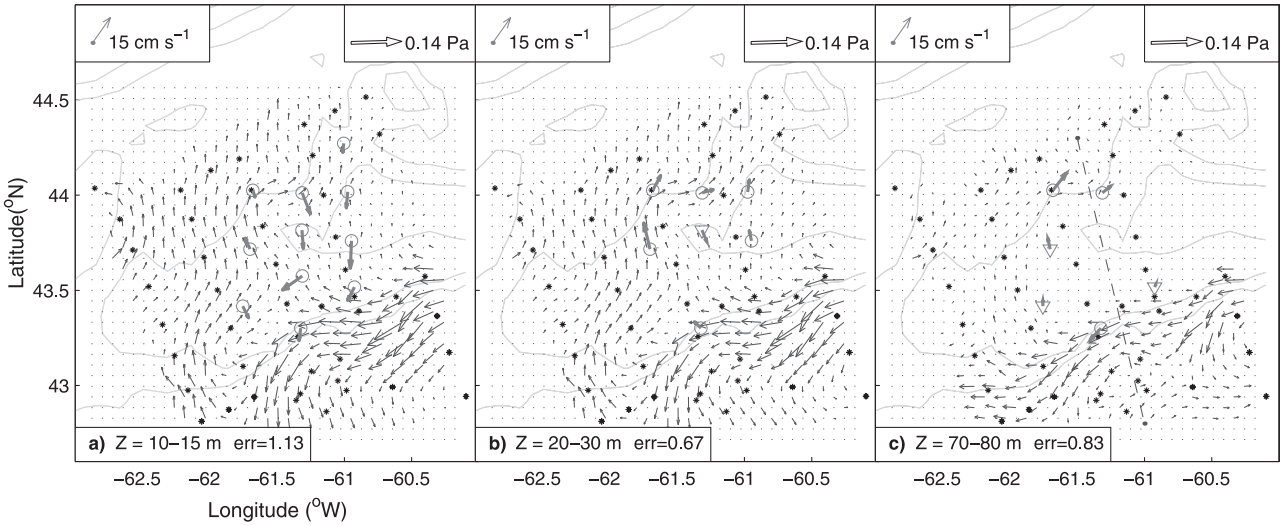

Figure 6. Velocity fields at (a) 12.5, (b) 25, and (c) 75 m depth for the first LSS obtained as a variational inverse of real (temperature, salinity, and velocity data). Asterisks: locations of used CTD profiles; circles: moorings with observed velocities on the correspondent depth. The triangle on Figure 6b subplot corresponds to the current meter deployed at 20 m depth. Triangles on Figure 6c subplot corresponds to the current meter deployed at 55 m depth. Solid arrows: averaged for the period of LSS subtidal velocities. Velocity scale, depths, and relative error between the real and modeled currents are shown at the top and bottom of each plot. The dashed line marks the position of density transect. The 0-, 50-, 100-, and 200-m isobaths are shown with the solid lines. The mean wind stress for the period is shown in the top left corner.

Analysis of 5-day, running means of the velocity data set from the 11 moorings reveals that spatial velocity variance is 2–5 times greater then the local velocity variance (Figure 5c). The dominance of the spatial over the local velocity variance suggests that the local current structure has some persistent large-scale features that may be treated as quasi-stationary for 5–7 days. Nonetheless, the local variability is not negligible, thus limiting the potential quantitative agreement of the quasi-stationary description.

3.3. Sequential Application of the Variational and Nonlinear Model for the First LSS

[36] We began by assimilating data from 29 September to 6 October using the variational algorithm. As a first guess, we interpolated temperature and salinity data onto a regular grid with a Gaussian correlation function $\rho\,(r,t) = \exp(-r^2/L^2 - t^2/T_{ad}^2)$. The horizontal resolution in both models was roughly 6 km. In the vertical, we had 26 layers, not all equal, with a minimum spacing of 4 m in the upper 20-m layer. The choice of smoothing scales of L = 20 km, T_{ad} = 8 days allowed us to avoid oversmoothing and permitted some consideration of the distribution of the data in time, for example, the data measured at the beginning and at the end of the survey allowed more model-data misfit than data from the middle of the survey. Estimates of the standard deviation of temperature and salinity varied from 10% to 25% of the observed mean variance at different depths.

[37] From the density data, we estimated the dynamic height, to be used as pseudo-data for SSH, relative to 500 m calculated following *Sheng and Thompson* [1996]. As discussed above, we estimate that the standard deviation of the dynamic height estimate is roughly 0.05 m. This error is large relative to the range of the dynamic height, which was about 0.1 m. To account for this large relative error, we set the corresponding SSH error covariance to permit a substantial "slack" for changes of SSH inside the variational model. We assume that the SSH error covariance was uniformly distributed.

[38] Averaged over the period of the first LSS, the velocities from the subsurface (deeper than 20 m) current meters were assimilated with the standard deviation based upon analysis of the subtidal velocity data. The standard deviation of the subtidal velocities was about 100% of the mean velocities in the surface (10–14 m) layer and ranged from 10–50% at subsurface (28–32 m) and deeper (55–75 m) levels.

[39] The standard deviation of the wind stress amplitude was about 50% of the mean wind stress. We set the surface fluxes to zero. Zero fluxes of heat and salt at the surface are reasonable, as the air and water temperature were roughly the same and there was no substantial precipitation during the cruise.

[40] We are able to compare results from the variational model (Figure 6) for the first LSS with the observed currents. The mean relative error $(rms(U - U_d) + rms(V - V_d))/(rms(U_d) + rms(V_d))$ between the modeled U,V and measured U_d,V_d velocities is shown for each simulation. The significant difference in the surface (10–15 m) layer is a result of the overly simplified representation of the surface circulation in the variational model. The poor agreement at 70–80 m is likely a consequence of the inadequate prescription of the barotropic velocity. Proper definition of the latter is constrained by the lack of sea surface elevation data, although we did use dynamic height data, and the absence of current meters on the western part of the Bank. The most serious drawback of the model field is the weak current on

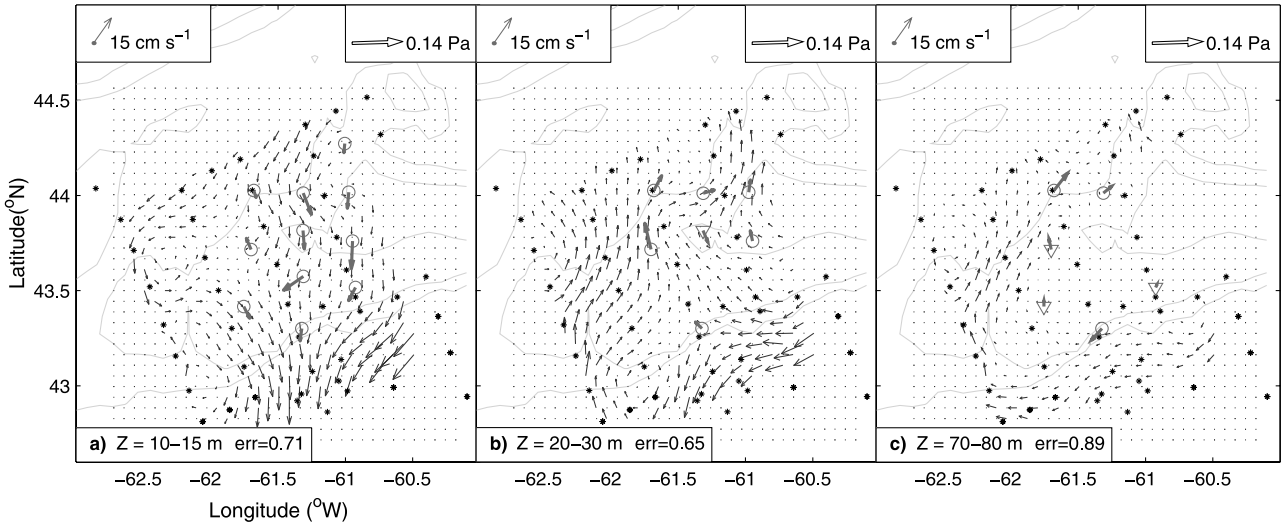

Figure 7. Diagnostic velocity fields at (a) 12.5, (b) 25, and (c) 75 m depth for the first LSS calculated using the variational model output. For details of the legend, see Figure 6.

the northern flank of Western Bank. At the same time, the current at Mooring 1 (see Figure 1) has a mean amplitude of about 0.1 m s^{-1}. We note that modeling studies of the climate circulation [*Hannah et al.*, 2001] on Western Bank also revealed strong circulation north of Western Bank.

[41] The output from the data assimilation model (velocity, temperature, and salinity) was used as input to the diagnostic, nonlinear primitive equation model [*Semenov and Luneva*, 1996, 1999]. Comparison of the diagnostic flow field (Figure 7) with the variational velocity fields (Figure 6) reveals strong improvements of the surface (10–15 m) circulation and intensification of the current in the northwest part of the investigated region. The reduction of the current amplitude on the southern flank yields better agreement with observations particularly if we look at the weak (about 1 cm s^{-1}) northeastern current measured at mooring 11 at 55 m depth (marked by the triangle on Figures 6c and 7c). There was little change in the errors between the modeled and observed velocity in the subsurface levels but there was a substantial reduction in the surface error (Figures 6a and 7a). Note that the velocity field exactly satisfies the nonlinear momentum and continuity equations. We speculate that the changes in the circulation are a consequence of inclusion of the $\kappa - \varepsilon$ turbulent closure scheme and application of the strong constraint in the nonlinear model which guarantees conservation of momentum and mass instead of the weak constraint approach of the variational model. It may also be that including the nonlinear terms has some influence.

[42] For the next step, the surface elevation and velocity fields at three depths (25, 55, and 75 m) were determined from the output of the nonlinear diagnostic model. These data were then fed back into the variational model to provide additional "simulated" data for that model while the previous estimates of the SSH were ignored. This represents the outer iteration cycle of the process (Figure 2). Results for the first LSS showed a positive influence of the proposed algorithm on the first, second, and third outer iterations. Further sequential application of the scheme caused some deterioration in the agreement between the modeled and measured velocities. Small non-physical eddies also developed that may be a consequence of the non-stationarity and/or some noise (internal tides for example) in the observations. This "noise" may not reveal itself in the variational model because of the weak constraint approach, but may be amplified after a number of iterations through the nonlinear model. The differences between the nonlinear and variational models can also cause "overfitting" of the simulated data from the nonlinear model.

[43] The variational and nonlinear velocity fields obtained after the third outer iteration (Figures 8 and 9) compared with the fields from the first outer iteration (Figures 6 and 7) reveal the smallest mean error between the modeled and real velocities. In the subsurface layers (20–30 m and 70–80 m), this improvement is seen in both the variational (Figures 6b, 6c, 8b, and 8c) and nonlinear (Figures 7b, 7c, 9b, and 9c) velocity fields. Some reduction in the goodness of fit to the observations in the surface layer (Figures 7a and 9a) may be partly compensated for by better agreement with observations at the second mooring (Figure 1) and may be explained by the large variance of subtidal currents at the surface.

[44] The major qualitative differences between the first and third outer iterations are an intensified inflow between Emerald and Western Banks, an increase of the eastward current on the northern flank of Western Bank, and a decrease of the along-slope current south of the Western Bank. All these features are consistent with the influence of strong topographic steering around Western Bank [*Han et al.*, 1998], and the strong (about 0.1 m s^{-1}) currents observed at the first (71 m) and second (30 m) moorings (Figure 1) and the weak northward current observed at the eleventh (55 m) mooring during the first LSS. It is interesting to note that the weak onshore component of the alongslope current (Figure 8c) originally appeared in the nonlinear diagnostic calculation during the first outer iteration (Figure 7c) but was later amplified during the third iteration. The strong influence of the nonlinear model on the final result likely follows from the $\kappa - \varepsilon$ turbulent closure

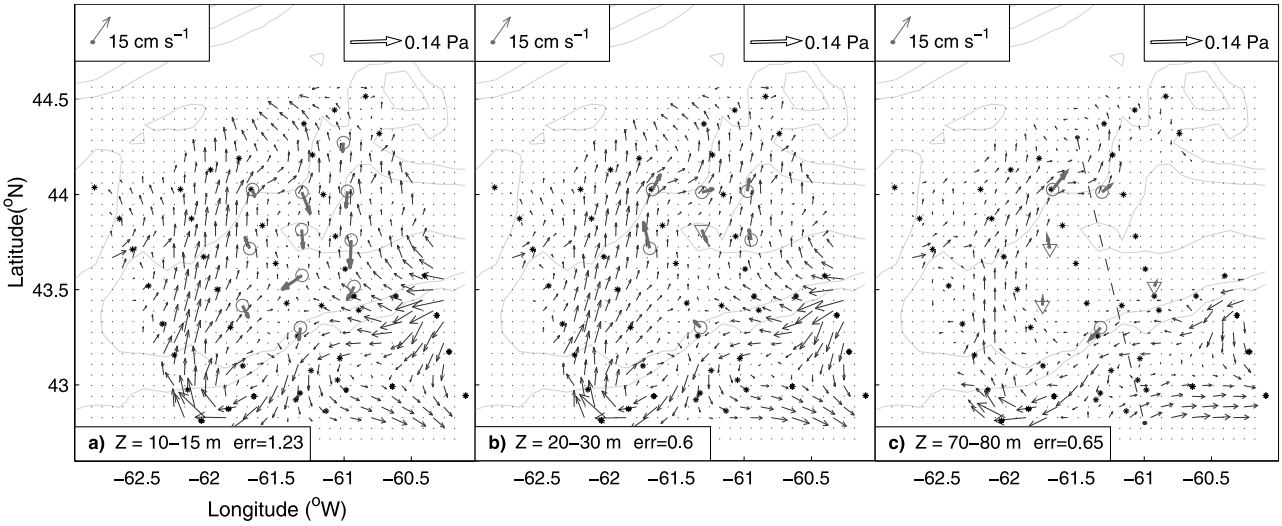

Figure 8. Velocity fields at (a) 12.5, (b) 25, and (c) 75 m depth for the first LSS obtained as a variational inverse of real (temperature, salinity, and velocity) and simulated data (SSH and velocity) on the third outer iteration. For details of the legend, see Figure 6.

scheme, the strong constraints of the nonlinear model and perhaps the inclusion of nonlinear terms in the momentum balance.

[45] The intensified current on the northern side of the Bank corresponds to the slope of the 26.0–26.45 isopycnals at 80–100 m (see Figures 10a and 10b). This current should reduce the density on the northern side of the bank, in agreement with the observed difference in density between the northern and southern sides of the bank (Figure 4).

[46] An increase of density below 70 m depth, and corresponding tilting of the isopycnals on the southern part of the transect, is in agreement with an intensification of the eastward current after the third outer iteration near 43°N and 60.5°W (Figures 8 and 6). Such an eastward current is similar to results obtained by *Han et al.* [1997]. Given these positive density changes, we can see that sequential application of the variational and nonlinear models can cause small but significant changes in the temperature and salinity structure. As the variational model produces dynamically balanced fields, these changes are accompanied by changes in the open boundary conditions, both helping to improve the realism of the circulation, particularly over such a small domain.

[47] Direct application of the nonlinear model to calculate the diagnostic flow field revealed strong sensitivity to specification of the open boundary conditions. The most physically reasonable result was developed after many numerical experiments and careful specification of the outflow velocity boundary condition by extrapolation from the internal points onto the open boundary and application of the zero integral transport correction. Application of the Orlanski radiation condition actually produced worse results. The inflow velocity boundary conditions were defined by using the modified dynamic method of [*Sheng*

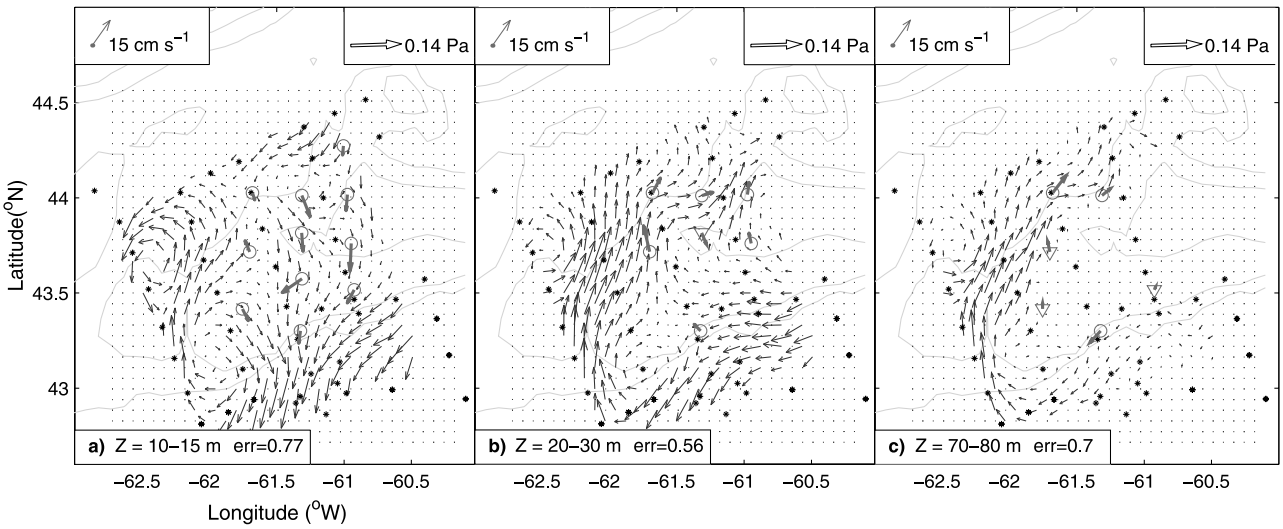

Figure 9. Diagnostic velocity fields at (a) 12.5, (b) 25, and (c) 75 m depth for the first LSS calculated using variational model output on the third outer iteration. For details of the legend, see Figure 6.

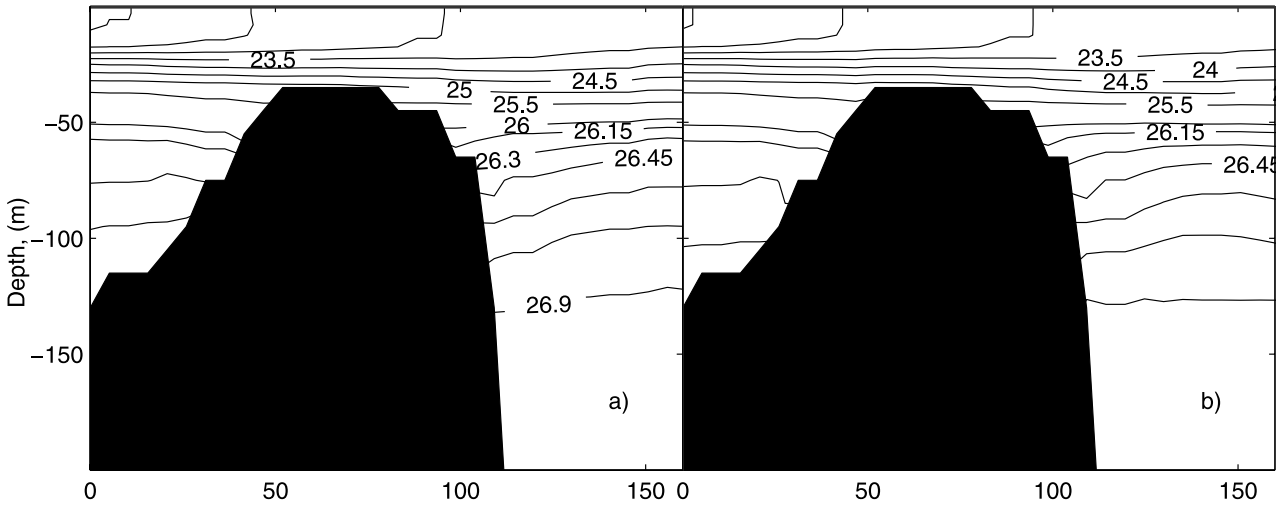

Figure 10. Contours of density along the transect marked by the dashed line dashed line shown in Figures 6c and 8c, after (a) first and (b) third outer iteration. The transect cuts across the edge of Western bank, running from the northwest to the southeast.

and Thompson [1996]. The errors between model and observed velocities were 0.85, 0.96, and 1.05 at 12.5, 25, and 75 m, respectively; that is. the error was greater than for the proposed approach. We did not present these results for two reasons: (1) The correlation function of the temperature/salinity distribution is unknown and thus we cannot check all the possible correlation functions. (2) There are many ways to apply open boundary conditions [*Orlanski*, 1976; *Greatbatch and Otterson*, 1991; *Shulman and Lewis*, 1995].

3.4. Quasi-Stationary Circulation of Western Bank

[48] The sequential approach was applied to the hydrographic data from the second LSS from 13 October to 20 October. Unfortunately, most of the moorings were recovered before 16 October, so we could not assimilate velocity data into the variational model. Nonetheless, we did use some velocity from a few moorings recovered from 15–17 October for comparison with the model results. The interaction between the two models was similar to that described above. The best agreement between the data and model (Figures 11 and 12) was after the third outer iteration (Figure 2). The nonlinear velocity field (Figure 12) provided the best fit to the observations. Although more detailed comparison between the observed and modeled currents was limited because of early recovery of the moorings, agreement with the truncated current observations is encouraging. For both the first and second surveys, the nonlinear flow field gave the best fit to the observed surface velocities and so we will use these results in our analysis of the circulation in the Western Bank (see Figures 9 and 12).

[49] At 10–15 m depth, the surface layer circulation shows major changes between the two surveys. During

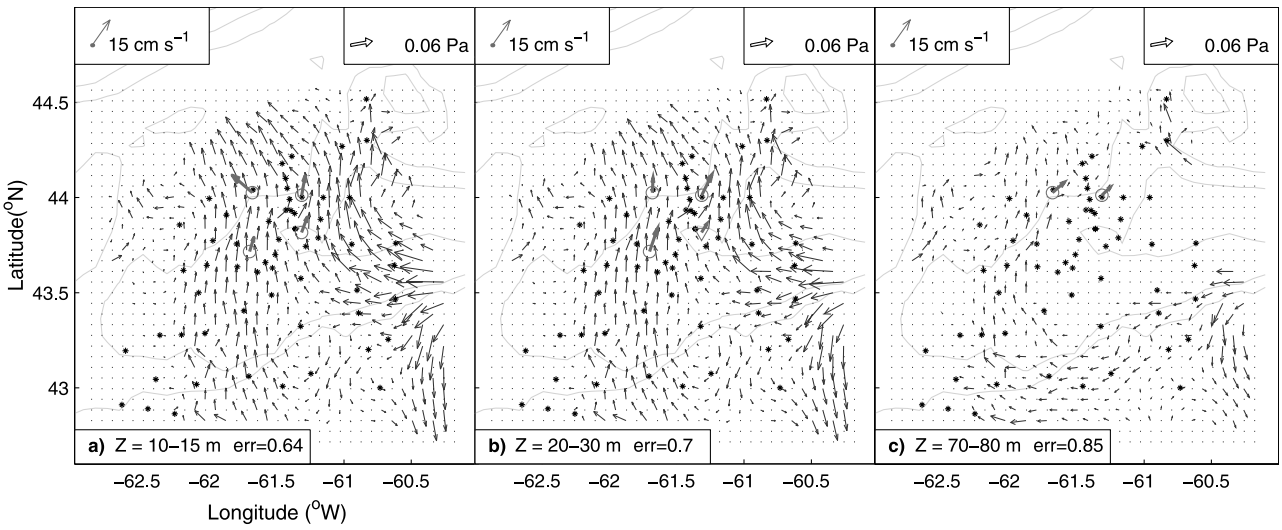

Figure 11. Velocity fields at (a) 12.5, (b) 25, and (c) 75 m depth for the second LSS obtained as a variational inverse of real (temperature, salinity, and velocity) and simulated data (SSH and velocity) on the third outer iteration. For details of the legend, see Figure 6.

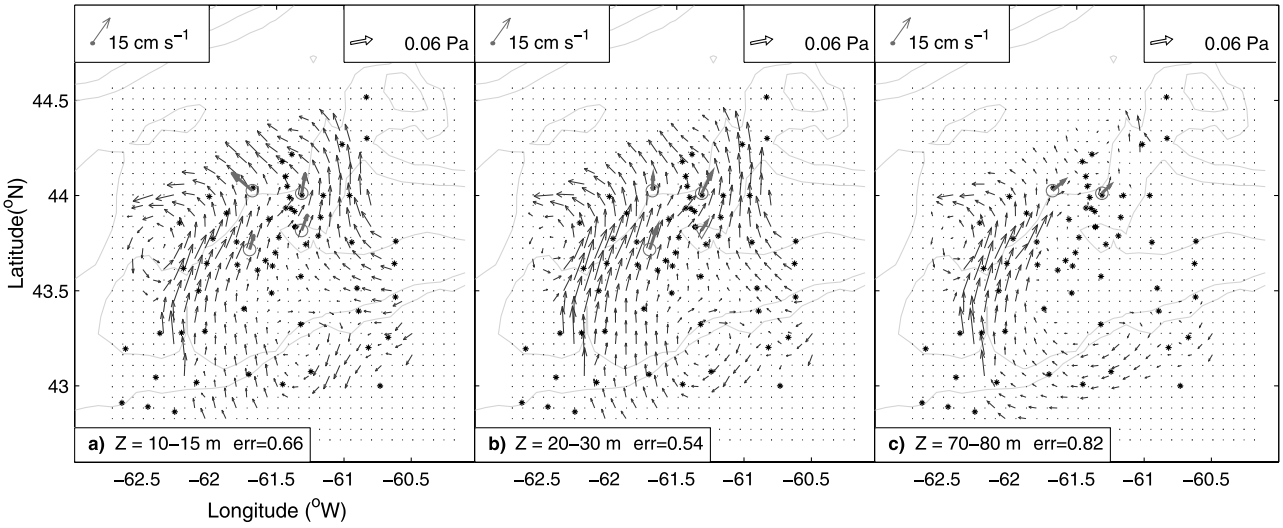

Figure 12. Diagnostic velocity fields at (a) 12.5, (b) 25, and (c) 75 m depth for the second LSS calculated using variational model output after the third outer iteration. For details of the legend, see Figure 6.

the first LSS, the surface current was primarily southward with velocities up to 0.1 m s^{-1} (Figure 9a). As mentioned above, the modeled northward current over the western half of the Bank agrees with the mooring observations. During the second LSS, the surface currents are primarily northward (Figure 12a). We speculate that these changes in the circulation followed the substantial shift in the wind stress during the period 10–16 October, with easterly winds shifting to westerly winds (Figure 3), and the weakness of the westerly wind in the latter half of the second LSS (16–20 October). The decrease of the westerly wind stress should reduce the southerly component of the surface wind-driven current, in agreement with the modeled and measured currents.

[50] The observed subsurface current, at 30 m (circles and solid arrows on Figures 9b and 12b), does not exhibit strong coherence with the wind stress, except at mooring 5 on the crest of the bank. Because of the shallow depth there (≈25 m), the current meter at this site was set at 20 m depth. The strong coherence there indicates the depth limitation of the surface wind stress. Nonetheless, the coherence between the velocity at different moorings (10- to 20-km separation) and different depths (30 m and 55 m) reflects large-scale changes in the Western Bank circulation probably associated with Ekman transport over the Scotian Shelf.

[51] Changes in the subsurface (20–30 m) circulation between the two surveys appear in the southern part of the domain. An along-slope, southwestward current of 0.1 m s^{-1} apparent in the first LSS (Figures 9b) shifted its core location southward after 12 days (Figures 12b), and its amplitude is reduced by 0.05 m s^{-1}. An intense anticyclonic mesoscale (roughly 40 km across) eddy moved eastward and offshore and its relative vorticity decreased. As a result, the inflow current concentrated near the westward channel during the first LSS became much broader and weaker (0.05 instead 0.1 m s^{-1}). On the basis of vorticity conservation arguments, the movement of the water onto the bank should be accompanied by a decrease in the strength of the relative vorticity. The observed offshore movement of the anticyclonic (negative vorticity) eddy effectively adds positive vorticity to the circulation on the bank. Since instability in shelf-break flows is quite common, and with the proposed link to the maintenance of the gyre over Western Bank, we suggest that these processes, involving the formation and offshore movement of the anticyclonic eddy, may play a key role in the exchange of momentum and water in this region of the Scotian Shelf.

[52] The reduced strength of the current over the southern half of the bank was accompanied by an intensification of the subsurface circulation to the west and the north. With the northward currents in the surface layer (during the second LSS), this intensification swept water from Western Bank. Analysis of samples collected after the second survey in October 1998 indicated that near the crest of the Western Bank, larval concentration were extremely low (<1 per 100 m^3), suggesting that larvae were advected off the bank. Salinity changes during this period (Figures 13a and 13b at 55 m depth) support this interpretation.

[53] Circulation at 70–80 m depth (Figures 9c and 12c) was more stable than nearer the surface but did also show some temporal evolution. For example, the offshore movement of the anticyclonic eddy allowed inshore penetration over much of Western Bank below 75 m depth. During the first LSS, the inflow was primarily concentrated in the channel region. There was also an intensification of the relatively strong (≈0.05 m s^{-1}) inflow into Emerald basin trough the channel between Western Bank and Middle Bank (see Figures 9c and 12c).

[54] The onshore transport, as determined from the nonlinear velocity fields, through the line *T* (Figure 1) was about 0.2 Sv and 0.35 Sv during the first and second LSS, respectively. This substantial increase in the onshore transport should lead to enhanced onshore transport of more saline water over the continental slope. The increase in salinity of 0.2 on line T on the north side of the bank at 55 m depth (Figure 13) between the two surveys supports this interpretation.

[55] Neither the model results nor the current observations revealed a closed anticyclonic circulation in the

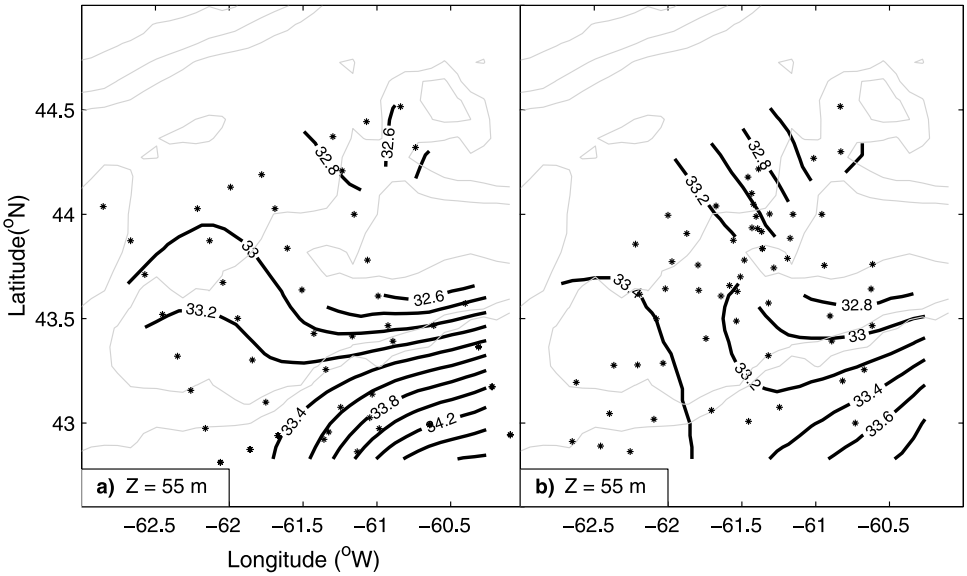

Figure 13. Salinity fields on 55 m for the (a) first and (b) second LSS calculated using variational model output after the third outer iteration.

subsurface flow around the crest of Western Bank. For this period at least, the closed anticyclonic circulation is limited to the surface layers, down to depths of 15–20 m. The Scotian Shelf region is characterized by a seasonal mean wind that is predominantly westerly [*Thompson and Hazen*, 1983], northwesterly in the winter, southeasterly during the summer, and purely westerly during the spring and fall. Analysis of the circulation during the first LSS shows that these winds generate a southward Ekman transport in the surface layer (Figure 9a). Combined with persistent onshore subsurface currents (Figure 9b), there is an associated closed circulation around Western Bank at intermediate depths, and as a consequence, conditions are generally favorable for biological retention on the bank [*O'Boyle et al.*, 1984; *Lochmann et. al.*, 1997; *Reiss et al.*, 2000]. Numerical modeling for the winter [*Hannah et al.*, 2001] and late fall [*Panteleev et al.*, 2001] circulation of the Scotian Shelf show similar closed circulation in the subsurface layer (to 40–50 m) over the crest of Western Bank. The spatial and vertical scale of the proposed closed circulation must be a function of wind stress amplitude. The circulation during the second LSS, following a period of strong easterly winds may be an example of the violation of the Western Bank system equilibrium and clearly leads to substantial qualitative and quantitative changes in the circulation.

4. Discussion and Conclusions

[56] The sequential algorithm presented here, involving the assimilation of diagnostic model data into the variational model is a variant on the standard approach of incorporating prior knowledge in data assimilation problems [*Thacker and Long*, 1988]. Where there are multiple local minima of the cost function and there is relatively large variance of the observed data, the assimilation of simulated data (if close to reality) should improve convergence towards the global minimum, the most physically realistic result. Here, studying a bank of a continental shelf, the bottom topography should substantially limit the range of possible solutions. The diagnostic calculation with the nonlinear model should lead to an improvement over the direct dynamic height approach [*Sheng and Thompson*, 1996]. The structured iteration cycle gradually incorporates the real features of the circulation of Western Bank as defined by the nonlinear model.

[57] The interaction between the variational and nonlinear models is somewhat complicated, and the implementation of the algorithm as presented here requires physical interpretation of the local oceanography of the Scotian Shelf. We use that knowledge to specify the error covariance for the newly simulated data and determine the improvement of the output of nonlinear model over the simplified variational model with relatively sparse data and only proxy SSH data. Determination of the end point for the iteration cycle also requires the application of some subjective judgment. Here, because we have independent velocity measurements, we could determine fairly easily when to stop the iteration.

[58] The initial convergence mentioned above and the divergence of the modeled velocity fields from real data can be explained qualitatively. Suppose a state vector P_{real} of the "real" quasi-stationary state of the ocean can be represented as

$$P_{dvar} = P_{real} - P_{var} \quad , \quad P_{dnon} = P_{real} - P_{non}, \qquad (2)$$

where, P_{var} is the maximum part of P_{real} which can be defined by the variational model, and P_{dvar} represents the mismatch between the two; P_{non} is the solution of the nonlinear model and P_{dnon} represents the mismatch with P_{real}. Because scaling analysis suggests that nonlinearity should be weak, then we expect $P_{var} \gg P_{dvar}$. If the solution of the variational problem after the ith iteration P^i_{var} (Figure 6) is far from P_{var} and if the solution of ith nonlinear problem P^1_{non} (Figure 7) is "better," then we should expect convergence of P^i_{var} to P_{real}. However, after a number of outer iterations, the sequential attraction to P_{non} can accumulate P_{dnon} and/or P_{dvar}, which cannot then be

described within the framework of the simplified variational model, nor can it be smoothed, and thus may be a source of errors. In our case, the sequential assimilation of nonlinear SSH could accumulate ζ_{dnon} and ζ_{dvar} and cause nonphysical errors, which will be adopted or smoothed if the momentum constraint of the variational model has nonlinear terms and the continuity equation plays an important role.

[59] The influence of the accumulation of $P_{dadd} = P_{dvar} + P_{dnon}$ during the iterative process may be avoided by convergence towards the observed data P_{ob}. Then, as in the case of assimilation of real P_{ob} and simulated P_{new}, the result will be equivalent to the assimilation of the

$$P_d = \left(\sigma_{ob}^{-1} P_{ob} + \sigma_{new}^{-1} P_{new}\right)\left(\sigma_{ob}^{-1} + \sigma_{new}^{-1}\right)^{-1}, \tag{3}$$

with covariance $\sigma_d = (\sigma_{ob}^{-1} + \sigma_{new}^{-1})^{-1}$. If the covariance of the newly simulated data σ_{new} is defined by equation (1), then the difference $|P_d - P_{ob}|$ will be limited, and for the weak nonlinearity of the variational model the result of the variational calculation should be also limited. Unfortunately convergence is not guaranteed.

[60] Like most oceanographic studies, our data set was incomplete. We did not have real SSH data, and the velocity observations were concentrated over the eastern part of our region, so we did not have a limit guaranteed by equation (3). But for the problem of the large-scale climate circulation, there are usually TOPEX/Poseidon SSH data, whose incorporation would help to constrain the variational model according to equation (3).

[61] This algorithm represents an attempt to combine the advantages of variational data assimilation approaches based on simplified governing equations and diagnostic calculations made with a fully nonlinear numerical model. The proposed algorithm does generate significant improvement for both the variational and nonlinear models. Depending upon the application, one model or the other might be the more useful endpoint for the iteration cycle. For applications where a detailed description of surface layer dynamics or the nonlinearity of the dynamical equations is important, then the results from the fully nonlinear model will be preferable. As was shown, the calculation with the nonlinear model is much better, particularly for the surface layer circulation.

[62] At the same time, because of the fixed temperature and salinity fields, the solution of the diagnostic problem is dynamically different from the quasi-stationary solution of the variational model. For some climate studies, it may be more useful to use output from the variational model rather than the nonlinear model (pathway 2 in Figure 2). In such studies, we often need to determine the quasi-stationary state of the ocean. Both the temperature/salinity and velocity fields should be stationary, and the degree of stationarity (see Appendix A) should have clear physical and mathematical meaning [see *Grotov et al.*, 1998]. In this situation it may be that there is no requirement to carefully resolve upper surface layer and the influence of nonlinearity is often negligible. Of course, the result will be quasi-stationary only in the context of the simplified dynamical constraints.

[63] As with many problems, the question of which model to use depends upon the problem being investigated. For application to Western Bank, the output from the nonlinear model is obviously preferable (pathway 1 in Figure 2). Using this approach, we have identified some qualitative conclusions about the Western Bank circulation for October 1998: (1) The cross slope transport over the Bank was about 0.2 Sv but the transport can double in periods of 5–10 days with sudden changes in wind conditions; (2) the decrease of the westerly winds and especially influence of the easterly wind is critical for the circulation over the Bank, and as a consequence important for resident biological populations [*Reiss et al.*, 2000]; and (3) vorticity conservation and wind forcing are proposed as physical features and mechanisms leading to the equilibrium anticyclonic structure of the Western Bank circulation.

[64] We have worked using existing models and algorithms and were bound by relatively strong quasi-stationary assumptions. The development of time-dependent models for the variational and diagnostic models is a subject for future work. The implementation of more classical variational [*Le Dimet and Talagrand*, 1986] and incremental [*Courtier et al.*, 1994; *Thompson et al.*, 2000] approaches, although preferable in principle, is undoubtedly quite complicated in practice.

Appendix A: Data Assimilation Algorithm

[65] The model underlying the data assimilation scheme was proposed by *Nechaev et al.* [1997], and is based upon standard formulations for the dynamical equations that include the effects of diffusivity of temperature, salinity and momentum and also accounts for the processes of vertical convective adjustment.

$$\rho - \mathcal{R}(\theta, S, p) = 0, \tag{A1}$$

$$p_z + g\rho = 0, \tag{A2}$$

$$f(\mathbf{k} \times \mathbf{u}) + \frac{1}{\rho_0}\nabla p - D_m \Delta \mathbf{u} - (K_m \mathbf{u}_z)_z = 0, \tag{A3}$$

$$\nabla \cdot \mathbf{u} + w_z = 0, \tag{A4}$$

$$\nabla \cdot (\mathbf{u}\theta) + (w\theta)_z - (K_\theta \theta_z)_z - D_\theta \Delta\theta - \hat{\Pi}_\theta \theta = F_\theta^e, \tag{A5}$$

$$\nabla \cdot (\mathbf{u}S) + (wS)_z - (K_S S_z)_z - D_S \Delta S - \hat{\Pi}_S S = F_S^e, \tag{A6}$$

where $\mathbf{u}$ is the horizontal velocity vector, w is the vertical velocity, D_m, D_θ, D_S, K_m, K_θ, and K_S are the horizontal and vertical diffusion coefficients of momentum, potential temperature θ, and salinity S, respectively; f is the Coriolis parameter; ∇ is the horizontal gradient operator; Δ is the Laplacian operator; g is the acceleration due to gravity; $\mathbf{k}$ is the vertical unit vector; and ρ_0 is a mean density. $\mathcal{R}$ simply represents the equation of state for seawater rewritten from the *United Nations Educational*, *Scientific*, and *Cultural Organization* [1981] formulation in terms of θ, S and p by *Ishizaki* [1994]. The fields of F_θ^e, F_S^e account for poorly known errors in parameterization of the mixing processes and for temperature and salinity evolution at timescales longer than some prescribed period T^*. The operator $\hat{\Pi}$ describes the vertical convection processes [see *Grotov et al.*, 1998, Appendix].

[66] Boundary conditions are applied at the surface, the bottom, and along the lateral boundaries. At the ocean surface $z = 0$, we impose the rigid-lid condition [*Gill*, 1982] and specify the fluxes of momentum, potential temperature, and salinity:

$$w = 0,$$

$$p - \rho g \zeta = 0,$$

$$K_m \mathbf{u}_z - \boldsymbol{\tau} = 0,$$

$$K_\theta \theta_z - B_\theta = 0,$$

$$K_S S_z - B_S = 0.$$

Here ζ, $\boldsymbol{\tau}$, B_θ, and B_S are surface elevation, wind stress, surface heat, and salt fluxes.

[67] At the ocean bottom the normal flow, the potential temperature, and the salinity fluxes are set to zero.

$$(D_\theta \nabla \theta + \mathbf{k} K_\theta \theta_z) \cdot \mathbf{n} = 0,$$

$$(D_S \nabla S + \mathbf{k} K_S S_z) \cdot \mathbf{n} = 0,$$

$$\mathbf{u} \cdot \nabla H - w - F^w = 0,$$

where $\mathbf{n}$ is a normal to the ocean bottom vector. Note that the last condition is not satisfied exactly. The error level F^w has the order of magnitude of the uncertainty of the Ekman pumping rate into the bottom boundary layer.

[68] At the rigid lateral boundaries, the momentum and tracer fluxes are set to zero. At the open boundaries, we neglect the diffusive fluxes for momentum, setting the velocities to be purely geostrophic and control the values of θ and S, determining them from the data through the inversion algorithm.

[69] The inversion algorithm is formulated in terms of the Gaussian probability distribution defined on the data space whose constituents are treated as stochastic Δ-correlated functions with unknown means [*Thacker*, 1989]. All the data components can be defined within the framework of the dynamical equations (A1)–(A6) in terms of the control fields θ, S, ζ, $\boldsymbol{\tau}$, and $B_{\theta,S}$.

[70] Our goal is to find the optimal set that minimizes the following argument of the Gaussian exponent:

$$\begin{aligned}
\mathcal{J} = & \int_\Omega \left\{ W_\theta (\theta - \theta^*)^2 + W_s (S - S^*)^2 \right\} d\Omega \\
& + \int_{z=0} \left\{ W_\theta^B \left(B_\theta - B_\theta^*\right)^2 + W_S^B \left(B_S - B_S^*\right)^2 \right. \\
& \left. + W_\zeta (\zeta - \zeta^*)^2 + W_\tau (\tau - \tau^*)^2 \right\} d\omega + \sum_{data} \mathbf{W}_\mathbf{u} (\mathbf{u} - \mathbf{u}^*)^2 \\
& + \int_\Omega \left\{ W_S^s (\Delta S)^2 + W_\theta^s (\Delta \theta)^2 \right\} d\Omega + \int_{z=0} \left\{ W_{B_\theta}^s (\Delta B_\theta)^2 + W_{B_S}^s (\Delta B_S)^2 \right. \\
& \left. + W_\zeta^s (\Delta \zeta)^2 + W_\tau^s (\Delta)^2 + \mathbf{W}_\psi^s \left(\Delta \int_{-H}^{0} \mathbf{u} dz \right)^2 \right\} d\omega \\
& + \int_\Omega \left\{ W_\theta^t \left(F_\theta^e\right)^2 + W_S^t \left(F_S^e\right)^2 \right\} d\Omega + W_w \int_{z=-H} (F^w)^2 d\omega.
\end{aligned}$$

Here Ω is the domain occupied by the computational grid, $\int_\Omega d\Omega$, $\int_{z=0} d\omega$, and $\int_{-H} d\omega$ are integrals over domain Ω, surfaces $z = 0$, and $z = -H$; θ^*, S^*, B_θ^*, B_S^*, ζ^*, $\boldsymbol{\tau}^*$, and $\mathbf{u}^*$ are the data for temperature, salinity, surface heat flux, surface salt flux, surface elevation, wind stress, and velocity, respectively. Model counterparts of these data are obtained by linear interpolation from closely located model points. The weight functions W_θ, W_θ^s, W_θ^t, W_S, W_S^s, W_S^t, W_w, W_ζ, W_ζ^s, W_τ, W_τ^s, W_B, W_B^s, W_ψ, and W_α incorporate additional information on the variability of the corresponding fields. According to the variational algorithm formulation [*Thacker*, 1989], the functions W^{-1} represent the error covariance functions of the corresponding physical values. We took their structure to be diagonal (i.e., having zero cross correlation in space), with diagonal elements depending on space coordinates.

[71] Typical values of $W_{\theta,S}^{-1/2}$ do not exceed 25% of the local spatial variability of the corresponding θ or S data. Assumptions about the smoothness of the temperature and salinity fields take into account the sharper horizontal gradients of these fields observed near the coastline and the banks. Diagonal elements of $W_{\theta,S}^s$ fade near the coast and banks by an order of magnitude, allowing for less smoothing in these regions. The error terms $F_{\theta,S}^e$ are due to treatment of the transport equations in the "weak" form, and can be interpreted as a "degree of unsteadiness" of the solution. The magnitude of the error terms depend upon the weight functions $W_{\theta,S}^t$ whose elements were chosen to be inversely proportional to the horizontal variances of the temperature and salinity divided by the time-scale T^* that is 8 days. In practice, the error terms $F_{\theta,S}^e$ are small except near abrupt changes in topography. The variance in the mass exchange with the bottom boundary layer $W_w^{-1/2}$ was specified as a typical Ekman pumping rate. Since shelf regions are typically characterized by strong vertical mixing, we specified a relatively large "acceptable" level of the misfit in the bottom boundary condition with the vertical velocity, about 100 m yr^{-1} defined by estimates of relative vorticity approximately 1×10^{-6} s^{-1} and vertical diffusion 5×10^{-4} m^2 s^{-1}. The diagonal elements of W_ζ, W_ζ^s, and W_ψ^s were chosen to be inversely proportional to bottom relief gradients, that are important for regulating circulation around the topography.

$$W_\varphi = \left\{ \left[10^{-6} + (\nabla H)^2 \right] \int_S (\varphi^* - \bar{\varphi}^*)^2 dS \right\}^{-1}$$

$$\varphi^* = \{\zeta^*, \Delta\zeta^*, \Delta\mathbf{U}\} \quad \mathbf{U} = \int_{-H}^{0} \mathbf{u} dz.$$

Here an overbar denotes the average over the sea surface, and $\mathbf{U}$ is the net transport vector of the first-guess state.

[72] The constrained minimization of $\mathcal{J}$ was performed using a version of a quasi-Newtonian descent algorithm proposed by *Gilbert and Lemarechal* [1989]. A first-guess state was computed using the control variables specified by the data. Taking into account the nonlinearity of the problem, we minimized $\mathcal{J}$ in a way outlined by *Grotov et al.* [1998], gradually increasing the number of control variables starting with the surface elevation ζ and moving up to the full control vector $\{\theta, S, \zeta, \tau, B_\theta, B_S\}$ whose dimension (the number of grid points occupied by the control fields) was 42,603.

[73] **Acknowledgments.** This work was part of the GLOBEC Canada program a joint partnership funded by the Natural Sciences and Engineering Research Council and the Department of Fisheries and Oceans. We thank our colleagues in this program, in particular the other investigators of the Western Bank study.

References

Bretherton, F. P., R. E. Davis, and C. B. Fandry (1976), A technique for objective analysis and design of oceanographic experiments applied to MODE-73, *Deep Sea Res.*, *23*, 559–582.

Camerlengo, A. L., and J. J. O'Brien (1980), Open boundary condition in rotating fluids, *J. Comput. Phys.*, *35*, 12–35.

Courtier, P., J. N. Thepaut, and A. Hollingsworth (1994), A strategy for operational implementation of 4D-Var, using an incremental approach, *Q. J. R. Meteorol. Soc.*, *120*, 1367–1387.

Csanady, G. T. (1979), The pressure field along the western margin of the North Atlantic, *J. Geophys. Res.*, *84*, 4905–4915.

Delekluze, P., and V. B. Zalesniy (1996), The questions of numerical modelling of the equatorial dynamic, *Oceanologia*, *36*, 24–42.

de Young, B., R. J. Greatbatch, and K. B. Forward (1993), A diagnostic coastal circulation model with application to the Conception Bay, Newfoundland, *J. Phys. Oceanogr.*, *23*, 2617–2635.

Gandin, L. S. (1963), *Objective Analysis of Meteorological Fields*, 206 pp., Gidrometeorizdat, St. Petersburg.

Gilbert, J. C., and C. Lemarechal (1989), Some numerical experiments with variable storage quasi-Newton algorithms, *Math. Program.*, *45*, 407–455.

Gill, A. E. (1982), *Atmosphere Ocean Dynamics*, 662 pp., Academic, San Diego, Calif.

Greatbatch, R. J., and T. Otterson (1991), On the formulation of open boundary conditions at the mouth of a bay, *J. Geophys. Res.*, *96*, 18,431–18,445.

Griffin, D. A., and K. R. Thompson (1996), The adjoint method of data assimilation used operationally for shelf circulation, *J. Geophys. Res.*, *101*, 3457–3477.

Grotov, A. S., D. A. Nechaev, G. G. Panteleev, and M. I. Yaremchuk (1998), Large-scale circulation in the Bellingshausen and Amundsen seas as a variational inverse of climatological data, *J. Geophys. Res.*, *103*, 13,011–13,022.

Haidvogel, D. B., and A. Beckmann (1999), *Numerical Circulation Modelling*, 318 pp., Imperial Coll. Press, London.

Han, G., C. G. Hannah, J. W. Loder, and P. C. Smith (1997), Seasonal variation of the three-dimensional mean circulation over the Scotian Shelf, *J. Geophys. Res.*, *102*, 1011–1025.

Hannah, C. G., J. A. Shore, J. W. Loder, and C. E. Naimie (2001), Seasonal circulation on the Western and Central Scotian Shelf, *J. Phys. Oceanogr.*, *31*, 591–615.

Helland-Hansen, B. (1934), *The Sognefjord Section-Oceanographic Observations in the Northernmost Part of the North Sea and the Southern Part of the Norwegian Sea: James Johnstone Memorial Volume*, Proudman Oceanogr. Lab., Bidston Obs., Birkenhead, UK.

Holland, W. R., and A. D. Hirshman (1972), A numerical calculation of the circulation in the North Atlantic Ocean, *J. Phys. Oceanogr.*, *2*, 336–354.

Houghton, R. W., P. C. Smith, and R. O. Fournier (1978), A simple model for cross-shelf mixing on the Scotian Shelf, *J. Fish. Res. Board Can.*, *35*, 414–421.

Ishizaki, H. (1994), A simulation of the abyssal circulation in the North Pacific Ocean, *J. Phys. Oceanogr.*, *24*, 1941–1954.

Large, W. G., and S. Pond (1981), Open ocean momentum fluxes in moderate to strong winds, *J. Phys. Oceanogr.*, *11*, 324–336.

Launder, B. E., G. J. Reece, and W. Rodi (1975), Progress in the development of a Reynolds-stress turbulent closure, *J. Fluid Mech.*, *68*, 537–566.

Le Dimet, F. X., and O. Talagrand (1986), Variational algorithms for analysis and assimilation of meteorological observations: Theoretical aspects, *Tellus, Ser. A*, *38*, 97–100.

Legler, D. M., I. M. Navon, and J. J. O'Brien (1989), Objective analysis of pseudo-stress over the Indian Ocean using a direct minimization approach, *Mon. Weather Rev.*, *117*, 709–720.

Lochmann, S. E., C. T. Taggart, D. E. Griffin, K. R. Thompson, and C. R. Mailett (1997), Abundance and condition of larval cod (Gadus morhua) at a convergent front on Western Bank, Scotian Shelf, *Can. J. Fish. Aquat. Sci.*, *54*, 1461–1479.

Marchuk, G. I., and V. V. Penenko (1979), A study of the sensitivity of discrete models of atmospheric and oceanic dynamics, *Iz. Atmos. Ocean Phys.*, *15*, 785–789.

Mellor, G. L., and T. Yamada (1982), Development of a turbulent closure model for geophysical fluid problems, *Rev. Geophys.*, *29*, 851–875.

Nechaev, D. A., and M. I. Yaremchuk (1995), Application of the adjoint technique to processing of a standard section data set: World Ocean Circulation Experiment section S4 along 67°S in the Pacific Ocean, *J. Geophys. Res.*, *100*(C1), 865–879.

Nechaev, D. A., G. G. Panteleev, and M. I. Yaremchuk (1997), Circulation in the Amundsen and Bellingshausen seas derived from atmospheric and oceanic climatologies, *Okeanologia Moscow*, *37*, 654–663.

O'Boyle, R., N. M. Sinclair, R. J. Conover, K. H. Mann, and A. C. Kohler (1984), Temporal and spatial distribution of ichthyoplankton communities on the Scotian Shelf in relation to biological, hydrological and physiographic features, *Rapp P. V. Reun. Cons. Int. Explor. Mer*, *183*, 27–40.

Orlanski, I. (1976), A simple boundary condition for unbounded hyperbolic flows, *J. Comput. Phys.*, *21*, 251–269.

Panteleev, G. G., B. de Young, and M. I. Yaremchuk (2001), The mean summer and fall circulation of Western Bank on the Scotian Shelf, *Atmos. Ocean*, *39*, 127–144.

Petrie, B., K. Drinkwater, D. Gregory, R. Pettipas, and A. Sandstrom (1996), Temperature and salinity atlas for the Scotian Shelf and the Gulf of Maine, *Can. Tech. Rep. Hydrogr. Ocean Sci.*, *171*, 398 pp.

Reiss, C., G. Panteleev, C. T. Taggart, J. Sheng, and B. de Young (2000), Observations on larval fish transport and retention on the Scotian Shelf in relation to geostrophic circulation, *Fish. Oceanogr.*, *9*, 195–213.

Sanderson, B. (1995), Structure of an eddy measured with drifters, *J. Geophys. Res.*, *100*(C4), 6761–6776.

Sarkisyan, A. S. (1954), Calculation of the stationary wind driven currents in the ocean (in Russian), *Izv. Akad. Nauk USSR*, *6*, 669–675.

Sasaki, Y. (1970), Some basic formalisms in numerical variational analysis, *Mon. Weather Rev.*, *98*, 875–883.

Semenov, E. V., and M. V. Luneva (1996), Numerical model of tidal and thermohaline circulation of the White Sea, *Izv. Ross. Akad. Nauk*, *32*, 704–713.

Semenov, E. V., and M. V. Luneva (1999), Combined effects of tide, stratification, and vertical turbulent mixing on the formation of hydrophysical fields in the White Sea, *Izv. Ross. Akad. Nauk*, *35*, 660–677.

Sheng, J., and K. R. Thompson (1996), A robust method for diagnosing regional shelf circulation from scattered density profiles, *J. Geophys. Res.*, *101*, 25,647–25,659.

Shulman, I., and J. K. Lewis (1995), Optimization approach to the treatment of open boundary conditions, *J. Phys. Oceanogr.*, *25*, 1006–1011.

Shulman, I., J. K. Lewis, and J. G. Mayer (1999), Local data assimilation in the estimation of barotropic and baroclinic open boundary conditions, *J. Geophys. Res.*, *104*, 13,667–13,680.

Simpson, J. (1998), Tidal processes in shelf seas, in *The Sea, The Global Coastal Ocean, Processes and Methods*, edited by K. H. Brink and A. R. Robinson, pp. 113–150, John Wiley, New York.

Smith, P. C., and F. B. Schwing (1991), Mean circulation and variability on the eastern Canadian shelf, *Cont. Shelf. Res.*, *11*, 977–1012.

Thacker, W. C. (1987), Three lectures on fitting numerical model to observations, *External Rep. CKSS 87/E/65*, 64 pp., GKSS Forshung. Geesthacht, Geesthacht, Germany.

Thacker, W. C. (1989), The role of the Hessian matrix in fitting models to measurements, *J. Geophys. Res.*, *94*(C5), 6177–6196.

Thacker, W. C., and R. Long (1988), Fitting dynamics to data, *J. Geophys. Res.*, *93*(C2), 1227–1240.

Thompson, K. R., and D. A. Griffin (1998), A model of the circulation on the outer Scotian Shelf with open boundary conditions inferred by data assimilation, *J. Geophys. Res.*, *103*(C13), 30,641–39,660.

Thompson, K. R., and M. G. Hazen (1983), Interseasonal changes of wind stress and Ekman upwelling: North Atlantic, 1950–1980, *Can. Tech. Rep. Fish. Aquat. Sci.*, *1214*, 175 pp.

Thompson, K. R., and J. Sheng (1997), Subtidal circulation on the Scotian Shelf: Assessing the hindcast skill of a linear, barotropic model, *J. Geophys. Res.*, *102*(C11), 24,987–25,003.

Thompson, K. R., M. Dowd, Y. Lu, and B. Smith (2000), Oceanographic data assimilation and regression analysis, *Environmetrics*, *11*, 183–196.

United Nations Educational, Scientific, and Cultural Organization (1981), Tenth report of the joint panel on oceanographic tables and standards, *UNESCO Tech. Pap. Mar. Sci.*, *36*, 25 pp.

Wunsch, C. (1994), Dynamically consistent hydrography and absolute velocity in the eastern North Atlantic Ocean, *J. Geophys. Res.*, *99*(C7), 14,071–14,090.

Wunsch, C. (1996), *The Ocean Circulation Inverse Problem*, 442 pp., Cambridge Univ. Press, New York.

B. de Young and G. G. Panteleev, Department of Physics and Physical Oceanography, Memorial University of Newfoundland, St. John's, A1B 3X7, Canada. (bdeyoung@physics.mun.ca)

M. Luneva and E. V. Semenov, Shirshov Institute of Oceanology, Nakhimovsky Prospect 36, Moscow, 117218, Russia.

C. Reiss, Department of Oceanography, Dalhousie University, Halifax, Nova Scotia, B3H 4J1, Canada.